Supplemental Material: Stabilization of frequency dependent squeezing with bichromatic control of filter cavity length, alignment and incident beam pointing

Yuhang Zhao[1,2],* Eleonora Capocasa[3], Marc Eisenmann[2], Naoki Aritomi[2], Michael Page[2], Yuefan Guo[4], Eleonora Polini[5], Koji Arai[6], Yoichi Aso[2], Martin van Beuzekom[4], Yao-Chin Huang[7], Ray-Kuang Lee[7], Harald Lück[8], Osamu Miyakawa[1], Pierre Prat[3], Ayaka Shoda[2], Matteo Tacca[4], Ryutaro Takahashi[2], Henning Vahlbruch[8], Marco Vardaro[4,9,10], Chien-Ming Wu[7], Matteo Leonardi[2], Matteo Barsuglia[3], and Raffaele Flaminio[5,2]

[1] *Institute for Cosmic Ray Research (ICRR), KAGRA Observatory, The University of Tokyo, Kamioka-cho, Hida City, Gifu 506-1205, Japan*

[2] *National Astronomical Observatory of Japan, 2-21-1 Osawa, Mitaka, Tokyo, 181-8588, Japan*

[3] *Laboratoire Astroparticule et Cosmologie (APC), 10 rue Alice Domon et Léonie Duquet, 75013 Paris, France*

[4] *Nikhef, Science Park, 1098 XG Amsterdam, Netherlands*

[5] *Laboratoire d'Annecy-le-Vieux de Physique des Particules (LAPP), Université Savoie Mont Blanc, CNRS/IN2P3, F-74941 Annecy-le-Vieux, France*

[6] *LIGO, California Institute of Technology, Pasadena, California 91125, USA*

[7] *Institute of Photonics Technologies, National Tsing-Hua University, Hsinchu 300, Taiwan*

[8] *Institut für Gravitationsphysik, Leibniz Universität Hannover and Max-Planck-Institut für Gravitationsphysik (Albert-Einstein-Institut), Callinstraße 38, 30167 Hannover, Germany*

[9] *Institute for High-Energy Physics, University of Amsterdam, Science Park 904, 1098 XH Amsterdam, Netherlands and*

[10] *Università di Padova, Dipartimento di Fisica e Astronomia, I-35131 Padova, Italy*

(Dated: March 1, 2022)

We firstly discuss here the geometry of an optical cavity under misalignment. To keep cavity aligned, the implementation of automatic alignment system is required. In the case of our bichromatic automatic alignment system, we summarize here its optical and control loop design. After that, the details of the filter cavity detuning variation are given when the cavity is kept locked and re-locked. We also provide a simulation of detuning change due to alignment change and different green and infrared beam size. This simulation shows the necessity of considering such effect for estimating detuning change under bichromatic cavity control. About frequency dependent squeezing fit, we also provide a greater detail here. In the end, more details about how detuning change affects quantum noise reduction are given.

I. MISALIGNMENT OF OPTICAL CAVITY: OPTICAL AXIS TILT AND SHIFT

The tilt of cavity mirrors introduces cavity optical axis tilt or shift. To understand these effects, we take definitions from Ref. [1] and analyze cavity alignment in our filter cavity based on small-angle approximation, which works in our case for a mirror tilt magnitude of μrad. Fig. 1 shows the geometry of the cavity before and after cavity mirrors tilt. The cavity optical axis tilt θ is caused by input mirror tilt θ_1, and end mirror tilt θ_2. The distance between mirrors center of curvature d_R is defined based on input mirror radius of curvature R_1 , end mirror radius of curvature R_2, and cavity length L.

$$d_R = R_1 - (L - R_2) \tag{1}$$

The beam waist position relative to the input mirror is

$$z_1 = d_R/2 + (L - R_2) = \frac{R_1 - R_2 + L}{2} \tag{2}$$

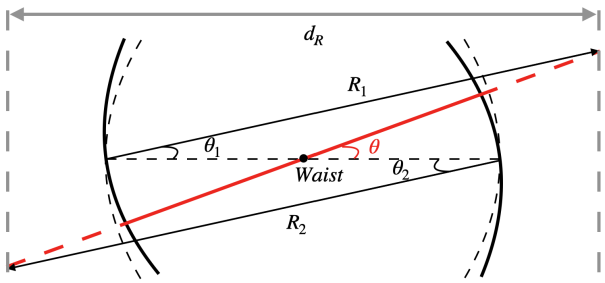

FIG. 1. Cavity geometry before and after optical axis tilt. The dashed lines show cavity mirrors and optical axis before tilt. The solid dark lines show cavity mirrors tilt with angles θ_1 and θ_2 for input and end mirrors separately. The solid arrow lines show cavity mirrors radius R_1 and R_2 for input and end mirrors separately. The red line shows the cavity optical axis after the optical axis tilt of θ. Finally, the grey lines indicate the distance between the mirror center of curvature d_R. Note that all these angles have a scale of μrad in our filter cavity.

The distance from the input mirror center of curvature to the original optical axis is $\theta_1 R_1$, and the distance from waist position to dashed grey line is $(R_1 + R_2 - L)/2$.

* Corresponding author:yuhang@icrr.u-tokyo.ac.jp

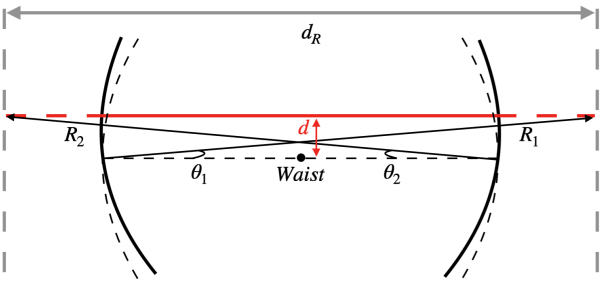

FIG. 2. Cavity geometry before and after optical axis shift. The dashed lines show cavity mirrors and optical axis before a shift. The solid dark lines show cavity mirrors tilt with angles θ_1 and θ_2 for input and end mirrors separately. The solid arrow lines show cavity mirrors radius R_1 and R_2 for input and end mirrors separately. The red line shows the cavity optical axis after the optical axis shift of d. Finally, the grey lines indicate the distance between mirrors center of curvature d_R. Note that all these angles have a scale of μrad in our filter cavity.

Therefore, we find

$$\theta = \frac{2\theta_1 R_1}{d_R} \tag{3}$$

We define here that a positive sign of mirror tilt angle is beam going up after reflection, as the input mirror of Fig. 1. If they have the same tilt directions, cavity optical axis shift will be introduced as Fig. 2. The cavity optical axis shift d is simply $R_1\theta_1$. We find that opposite direction of end mirror tilt introduces only cavity optical axis tilt or shift. Besides, θ_1 and θ_2 should satisfy relation $\theta_1 \mathrm{R}_1 = \theta_2 \mathrm{R}_2$. Therefore, the cavity optical axis tilt should be written as

$$\theta = \frac{\theta_1 R_1}{d_R} - \frac{\theta_2 R_2}{d_R}. \tag{4}$$

So that when input mirror tilt by a value proportional of R_2 and end mirror tilt by a value proportional of R_1, Eq. 4 becomes zero. Following the same principle, for cavity optical axis shift, we find

$$d = \frac{\theta_1 R_1}{2} + \frac{\theta_2 R_2}{2} \tag{5}$$

From Eq. 4 and Eq. 5, we find the cavity optical axis shift and tilt and mirrors tilt have relation as follows

$$\begin{pmatrix} \delta d \\ \delta\theta \end{pmatrix} = \begin{pmatrix} R_1/2 & R_2/2 \\ R_1/d_R & -R_2/d_R \end{pmatrix} \begin{pmatrix} \delta\theta_1 \\ \delta\theta_2 \end{pmatrix} \tag{6}$$

Considering Fig. 1 and Fig. 2, we find that when the cavity optical axis is tilted or shifted, cavity length can change. In the case of cavity optical axis tilt, as Fig. 3 , we can write cavity length change as

$$\begin{aligned} \delta\mathrm{L}_{\mathrm{tilt1}} &= \theta^2 z_1 = \theta^2 \frac{R_1 - R_2 + L}{2}, \\ \delta\mathrm{L}_{\mathrm{tilt2}} &= \theta^2 (L - z1) = \theta^2 \frac{L - R_1 + R2}{2}. \end{aligned} \tag{7}$$

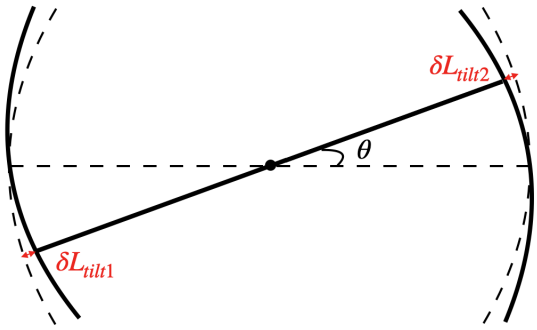

FIG. 3. Cavity length change caused by cavity optical axis tilt

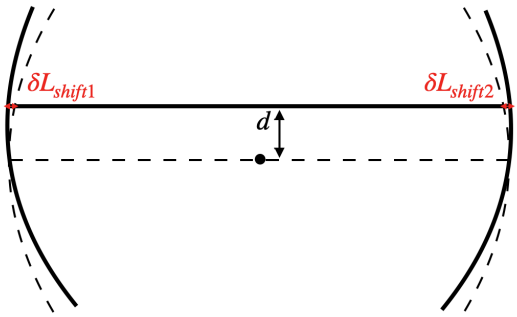

FIG. 4. Cavity length change caused by cavity optical axis shift

In the case of cavity optical axis shift, as Fig. 4 , we can write cavity length change as

$$\begin{aligned} \delta\mathrm{L}_{\mathrm{shift1}} &= \mathrm{d}\theta_1, \\ \delta\mathrm{L}_{\mathrm{shift2}} &= \mathrm{d}\theta_2. \end{aligned} \tag{8}$$

It can be seen that the tilted cavity length gets shorter as Fig. 3 and the shifted cavity length gets longer as Fig. 4. In the end, we find total cavity length change

$$\begin{aligned} \delta\mathrm{L} &= -\delta\mathrm{L}_{\mathrm{tilt1}} - \delta\mathrm{L}_{\mathrm{tilt2}} + \delta\mathrm{L}_{\mathrm{shift1}} + \delta\mathrm{L}_{\mathrm{shift2}} \\ &= (\frac{R_1}{2} - \frac{R_1^2 L}{d_R^2})\theta_1^2 + (\frac{R_2}{2} - \frac{R_2^2 L}{d_R^2})\theta_2^2 \\ &\quad + (\frac{2R_1 R_2 L}{d_R^2} + \frac{R_1 + R_2}{2})\theta_1\theta_2 \end{aligned} \tag{9}$$

II. WAVEFRONT SENSING AUTOMATIC ALIGNMENT PRINCIPLE

To correct the misalignment between cavity incident beam axis and cavity internal optical axis, the wavefront distortion of the cavity reflected beam can be utilized [2]. This wavefront distortion is caused by the interference between the reflected beam not coupled to cavity and the reflected beam coupled to cavity. We will go a bit into detail in this section, which tells us how to design our automatic alignment loop.

The beam, usually called carrier, going to an optical cavity needs to have itself pass through an EOM firstly. In this way, carrier will be phase modulated, and a pair of sidebands will be generated [3]. Using Pound-Drever-Hall locking technique, the carrier can be kept resonant inside an optical cavity. However, sidebands can be resonant or not depending on EOM phase modulating frequency and cavity free spectral range. The cavity reflectivity for carrier and sidebands will be a complex value and depends on frequency [3]. Due to the spatial overlap of carrier and sidebands, misalignment causes the generation of higher order modes for both carrier and sidebands. If the incident light axis and cavity axis have only slight lateral displacement and tilt, the reflected carrier can be approximately written as[4]

$$E^c_{ref} = (U_{00}r_{c0} + \epsilon U_{10}r_{c1})E_c e^{i\omega t} \tag{10}$$

where ϵ describes field coupling coefficient from fundamental mode U_{00} to the first higher order mode U_{10}, with $\epsilon = \frac{\delta d}{\omega_0} + i\frac{\delta\theta}{\theta_D}$. ω_0 is the radius of beam waist, and $\theta_D = \frac{\lambda}{\pi\omega_0}$ is the divergence angle of the fundamental mode. r_{c0} is the amplitude reflectivity for the fundamental mode of carrier, and r_{c1} is the amplitude reflectivity for the first higher mode of carrier. E_c is the incident carrier field amplitude. In the same manner, the reflected sidebands can be approximately written as

$$E^s_{ref} = (U_{00}r_{s0} + \epsilon U_{10}r_{s1})E_s e^{i(\omega\pm\Omega)t} \tag{11}$$

where Ω is the frequency of modulation. If we demodulate filter cavity reflection signal with a local oscillator having frequency of Ω, many terms of beat signals can be neglected, and we find

$$P_\Omega = E^c_{ref}E^{s*}_{ref} - E^{c*}_{ref}E^s_{ref} \tag{12}$$

The WFS signal is obtained by taking the differential signal of QPD's two half segments. Therefore, considering the expression of Hermite polynomials, the $U_{00}U_{00}$ and $U_{01}U_{01}$ terms will cancel out. By ignoring amplitude $E_{c/s}$ and phase $e^{i\Omega t}$ terms, we find

$$\begin{aligned} P_\Omega &= (U^*_{00}U_{10}\epsilon - U_{00}U^*_{10}\epsilon^*)(-r^*_{c0}r_{s1} + r_{c1}r^*_{s0}), \\ &= ((U^*_{00}U_{10} - U_{00}U^*_{10})\frac{\delta d}{\omega_0} + (U^*_{00}U_{10} + U_{00}U^*_{10})\frac{i\delta\theta}{\theta_D}) \\ &\quad (-r^*_{c0}r_{s1} + r_{c1}r^*_{s0}). \end{aligned} \tag{13}$$

Considering sidebands, sidebands higher-order modes and carrier higher-order modes are off-resonance, while the carrier is kept on resonance, we find

$$\begin{aligned} P_\Omega = ((U^*_{00}U_{10} - U_{00}U^*_{10})&\frac{\delta d}{\omega_0} \\ +(U^*_{00}U_{10} + U_{00}U^*_{10})&\frac{i\delta\theta}{\theta_D})(r_{c0}+1) \end{aligned} \tag{14}$$

We recall the expression of Hermite Gaussian modes

$$\begin{aligned} U_{mn} = U_m(x,z)U_n(y,z)& \\ exp[-ikz + i(m+n+1)\eta(z)]&, \end{aligned} \tag{15}$$

where

$$\begin{aligned} U_m(x,z) = (\frac{2}{\pi\omega^2(z)})^{1/4}\sqrt{\frac{1}{2^m m!}}& \\ H_m(\frac{\sqrt{2}x}{\omega(z)})exp[-(\frac{x}{\omega(z)})^2 - i\frac{kx^2}{2R(z)}]&, \end{aligned} \tag{16}$$

where H_m is the m-order Hermite polynomial with $H_0(x) = 1$ and $H_1(x) = x$, $\omega(z) = \omega_0\sqrt{1 + z^2/z_0^2}$ is the beam radius, $\eta(z) = \arctan(z/z_0)$ is the Gouy phase, $R(z) = z(1 + z_0^2/z^2)$ is the beam radius of curvature and $z_0 = k\omega_0^2/2$ is the Rayleigh range. Considering expression of Hermite Gaussian modes, we get

$$U^*_{00}U_{10} - U_{00}U^*_{10} = -2iU^*_1U^*_0U_0U_0\sin(\eta) \tag{17}$$

$$U^*_{00}U_{10} + U_{00}U^*_{10} = 2U^*_1U^*_0U_0U_0\cos(\eta) \tag{18}$$

Taking into the power terms, the demodulated filter cavity reflection signal will become

$$\begin{aligned} P^{WFS}_\Omega &= iP_0J_0(\beta)J_1(\beta)P_\Omega \\ &= -2P_0J_0(\beta)J_1(\beta)U^*_1U^*_0U_0U_0(r_{c0}+1) \\ &\quad [\frac{\delta d}{\omega_0}\sin(\eta) - \frac{\delta\theta}{\theta_D}\cos(\eta)], \end{aligned} \tag{19}$$

where$P_0J_0(\beta)J_1(\beta) = \sqrt{P_cP_s}$ is the filter cavity reflection power at frequency Ω with carrier power $P_c = J_0^2(\beta)P_0$ and sideband power $P_s = J_1^2(\beta)P_0$ expressed using Bessel functions. Integrating two half segments of the reflected power in x-y plane and taking their differential as $\int\int dxdy\{U^*_1U^*_0U_0U_0(x>0) - U^*_1U^*_0U_0U_0(x<0)\} = \sqrt{2/\pi}$, we get WFS signal

$$P^{WFS}_\Omega = -\sqrt{\frac{2}{\pi}}\beta P_0(r_{c0}+1)[\frac{\delta d}{\omega_0}\sin(\eta) - \frac{\delta\theta}{\theta_D}\cos(\eta)] \tag{20}$$

where $J_0(\beta)J_1(\beta) \simeq \beta/2$ was used considering a small phase modulation depth. If we put WFS sensors at $\eta = 0°$ and $\eta = 90°$ separately, the $0°$ sensor sense only tilt while the $90°$ sensor sense only shift. If we put WFS sensors at $\eta = -45°$ and $\eta = 45°$ separately, the common signal of two sensors senses the tilt while the differential signal of two sensors senses the shift. Although it is not mandatory to put two WFS sensors with a certain phase difference, a larger WFS signal can be acquired if they have a phase difference of $90°$.

Considering Eq. 6 and parameters in Table. I, we find the WFS signals based on cavity mirror's angular motion

$$\begin{pmatrix}\delta d \\ \delta\theta\end{pmatrix} = \begin{pmatrix}224.9 & 222.6 \\ 0.75 & -0.77\end{pmatrix}\begin{pmatrix}\delta\theta_1 \\ \delta\theta_2\end{pmatrix} \tag{21}$$

Taking Eq. 21 into Eq. 20, we find

$$\begin{aligned} P^{WFS}_\Omega = \sqrt{\frac{2}{\pi}}&\beta P_0(r_{c0}+1) \\ &\{[3.4\cos(\eta) - 2.4\sin(\eta)]\delta\theta_1 \\ &+[3.3\cos(\eta) + 2.4\sin(\eta)]\delta\theta_2\}. \end{aligned} \tag{22}$$

TABLE I. Summary of the filter cavity parameters.

Parameter	Symbol	Value
Length	L	300 m
Mirror radius	R	50 mm
Input mirror radius of curvature	R_1	436.7 m
End mirror radius of curvature	R_2	445.1 m
PARAMETERS FOR GREEN		
Input mirror transmissivity	T_1	0.7 %
End mirror transmissivity	T_2	2.9 %
Finesse	$\mathcal{F}$	172
Linewidth	Δ_ν	2905 Hz
Storage time	τ	0.11 ms
Beam radius at input mirror	w_1	7.26 mm
Beam radius at end mirror	w_2	7.35 mm
PARAMETERS FOR INFRARED		
Input mirror transmissivity	T_1	0.136 %
End mirror transmissivity	T_2	3.9 ppm
Finesse	$\mathcal{F}$	4425
Linewidth	Δ_ν	113 Hz
Storage time	τ	2.82 ms
Beam radius at input mirror	w_1	10.26 mm
Beam radius at end mirror	w_2	10.40 mm

This equation will be used to decide where we should put WFS sensors for filter cavity. For example, to make the WFS sensor only sensitive to the input mirror, we need to put it at 55°. Meanwhile, the other WFS sensor needs to be put at −54° to sense only the end mirror.

III. WAVE FRONT SENSING AUTOMATIC ALIGNMENT SYSTEM CONTROL LOOP DESIGN

From the calculation of WFS signals, it is clear that we need to set up two QPDs in the reflection of filter cavity with specific Gouy phases. While designing an optical setup, we also considered providing proper beams size for QPDs to avoid signal loss[5]. Assuming a QPD has only horizontal misalignment much smaller than beam radius, we have QPD response as a function of beam radius

$$S = \frac{\sqrt{2/\pi}}{\omega}\left(\mathrm{e}^{-\frac{2\mathrm{a}^2}{\omega^2}} - \mathrm{e}^{-\frac{2\mathrm{b}^2}{\omega^2}}\right) U \tag{23}$$

with

$$U = 2\mathrm{erf}\left(\frac{\sqrt{2}\mathrm{a}}{\omega}\right) - 2\mathrm{erf}\left(\frac{\sqrt{2}b}{\omega}\right), \tag{24}$$

where ω is the beam radius on QPD, a is the size of one segment of QPD, b is half of the QPD gap. In this experiment, using a commercial QPD (First sensor QP45-Q TO), we have a = 3.31 [mm] and b = 0.035 [mm]. Our QPD response to small misalignment as a function of beam radius on QPD is shown in Fig. 5. Considering this figure and the laser beam parameter, we chose beam radius of around 0.2 mm in the experiment.

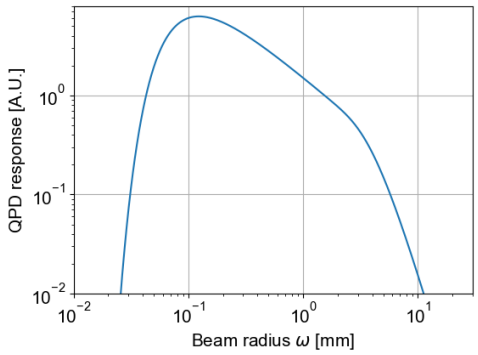

FIG. 5. QPD response as a function of ω. The response is divided by a factor of 1000 to have the peak value around 1.

The DC signals of the QPD four segments are acquired to center filter cavity reflected light on QPD. This pointing control is actuated by a galvanometer scanner[6]. After QPDs different segments RF signals are demodulated with optimal phase, their left and right half differential signals are used to extract mirrors yaw angular motion while their upper and lower differential signals are used to extract mirrors pitch angular motion. For filter cavity automatic alignment, four degrees of freedom motion are sensed by two QPDs, including input mirror pitch ($\mathbf{In_p}$), input mirror yaw ($\mathbf{In_y}$), end mirror pitch ($\mathbf{En_p}$), and end mirror yaw ($\mathbf{En_y}$). Correspondingly, two QPDs have four degrees of freedom sensing, including QPD1 pitch ($\mathbf{QPD_{1p}}$), QPD1 yaw ($\mathbf{QPD_{1y}}$), QPD2 pitch ($\mathbf{QPD_{2p}}$), QPD2 yaw ($\mathbf{QPD_{2y}}$).

In the experimental implementation, we can have two coupling issues for these different DOFs

- QPDs are usually not sensing input/end mirrors independently due to beam quality issues, QPDs placement error induced Gouy phase error and slightly different gain of the four segments of a QPD. Therefore, it is always required to combine two QPDs signals to reconstruct the input or end mirror angular motion.

- QPDs pitch and yaw can have coupling due to QPD rotation. Even if we could sense purely pitch and yaw WFS signal, the feedback actuators have pitch and yaw coupling.

To solve these coupling issues, we have developed a method. The first step is to characterize the WFS sensors' response to input/end mirrors angular motion. We drive filter cavity alignment four DOFs individually with a frequency far from mirror suspension system resonant frequencies to check this response. After that, we compute the transfer function spectrum from this driving signal to QPDs sensing signals. This transfer function measurement tells us the response magnitude and sign.

In this way, we find a 4×4 sensing matrix $\mathbf{M}$

$$\begin{pmatrix} \mathbf{QPD_{1p}} \\ \mathbf{QPD_{2p}} \\ \mathbf{QPD_{1y}} \\ \mathbf{QPD_{2y}} \end{pmatrix} = \mathbf{M} \begin{pmatrix} \mathbf{In_p} \\ \mathbf{En_p} \\ \mathbf{In_y} \\ \mathbf{En_y} \end{pmatrix} \tag{25}$$

By inverting matrix $\mathbf{M}$, we find the matrix to combine signals from QPDs different sensing DOFs and used to drive cavity mirrors. Furthermore, since the sensing matrix $\mathbf{M}$ includes the coupling information, the driving matrix $\mathbf{M}^{-1}$ can avoid coupling issues during the alignment control.

IV. DETAILS ON FILTER CAVITY DETUNING DRIFT DUE TO FILTER CAVITY LENGTH/LASER FREQUENCY DRIFT

In this section, we give more details about equations from the section three part A of the main manuscript.

A. Detuning drift when the cavity is kept locked

Here we provide more derivation from the main manuscript Eq. 3 to Eq. 4 and Eq. 5. Eq. 3 is written as

$$\Delta_{\mathrm{d}} = \frac{\mathrm{c} \cdot \delta_{\mathrm{AOM}}}{2\mathrm{L}\lambda_{\mathrm{green}}(\lambda_{\mathrm{green}} + \delta_{\mathrm{AOM}})}\delta\mathrm{L}. \tag{26}$$

Here, δ_{AOM} is expressed as

$$\begin{aligned} \delta_{\mathrm{AOM}} &= \frac{\mathrm{c}}{\mathrm{f_{green}}} - \frac{\mathrm{c}}{\mathrm{f_{green}} + \mathrm{f_{AOM}}} \\ &= \mathrm{c}\frac{\mathrm{f_{AOM}}}{\mathrm{f_{green}}(\mathrm{f_{green}} + \mathrm{f_{AOM}})} \\ &= \lambda_{\mathrm{green}}\frac{\mathrm{f_{AOM}}}{\mathrm{f_{green}} + \mathrm{f_{AOM}}}. \end{aligned} \tag{27}$$

Takeing this into Eq. 26, we obtain

$$\begin{aligned} \Delta_{\mathrm{d}} &= \frac{\mathrm{c}}{2\mathrm{L}}\frac{\lambda_{\mathrm{green}}\frac{\mathrm{f_{AOM}}}{\mathrm{f_{green}}+\mathrm{f_{AOM}}}}{\lambda_{\mathrm{green}}(\lambda_{\mathrm{green}} + \delta_{\mathrm{AOM}})}\delta\mathrm{L} \\ &= \frac{\mathrm{c}}{2\mathrm{L}}\frac{\frac{\mathrm{f_{AOM}}}{\mathrm{f_{green}}+\mathrm{f_{AOM}}}}{(\lambda_{\mathrm{green}} + \delta_{\mathrm{AOM}})}\delta\mathrm{L} \\ &= \frac{\mathrm{c}}{2\mathrm{L}}\frac{\frac{\mathrm{f_{AOM}}}{\mathrm{f_{green}}+\mathrm{f_{AOM}}}}{(\lambda_{\mathrm{green}} + \lambda_{\mathrm{green}}\frac{\mathrm{f_{AOM}}}{\mathrm{f_{green}}+\mathrm{f_{AOM}}})}\delta\mathrm{L} \\ &= \frac{\mathrm{c}}{2\mathrm{L}}\frac{\mathrm{f_{green}}}{\mathrm{c}}\frac{\frac{\mathrm{f_{AOM}}}{\mathrm{f_{green}}+\mathrm{f_{AOM}}}}{(1 + \frac{\mathrm{f_{AOM}}}{\mathrm{f_{green}}+\mathrm{f_{AOM}}})}\delta\mathrm{L} \\ &= \frac{\mathrm{f_{green}}}{2\mathrm{L}}\frac{\mathrm{f_{AOM}}}{\mathrm{f_{green}} + 2\mathrm{f_{AOM}}}\delta\mathrm{L} \\ &= \frac{\mathrm{f_{AOM}}}{2\mathrm{L}}\frac{\mathrm{f_{green}}}{\mathrm{f_{green}} + 2\mathrm{f_{AOM}}}\delta\mathrm{L} \\ &\simeq \frac{\mathrm{f_{AOM}}}{2\mathrm{L}}\delta\mathrm{L} \\ &= 1.83 \times 10^5[\mathrm{Hz/m}] \cdot \delta\mathrm{L}[\mathrm{m}]. \end{aligned} \tag{28}$$

The approximation is made by approximating $\mathrm{f_{green}} + 2\mathrm{f_{AOM}}$ to be $\mathrm{f_{green}}$, so that $\frac{\mathrm{f_{green}}}{\mathrm{f_{green}}+2\mathrm{f_{AOM}}}$ is unity. Since $\delta\mathrm{L} = (\mathrm{L/f}) \cdot \delta\mathrm{f} = (300/2.82 \times 10^{14}) \cdot \delta\mathrm{f} = 1.06 \times 10^{-12} \cdot \delta\mathrm{f}$, we have $\Delta_{\mathrm{d}} = 1.95 \times 10^{-7} \cdot \delta\mathrm{f}$.

B. Detuning shift after the cavity lock is lost and re-acquired

Initially, we assume that the cavity is locked on resonance for both infrared and green laser beams. We have

$$\mathrm{f_{green}} = 2\mathrm{f_{infrared}} + \mathrm{f_{AOM}} = \mathrm{N} \cdot \mathrm{FSR}.(\mathrm{N} \in \mathbb{Z}) \tag{29}$$

Here we have $2\mathrm{f_{infrared}} = \mathrm{M} \cdot \mathrm{FSR}(\mathrm{M} \in \mathbb{Z})$ and $\mathrm{f_{AOM}} = \mathrm{I} \cdot \mathrm{FSR}(\mathrm{I} \in \mathbb{Z})$. After the cavity loses lock and laser frequency change by Δf, the green laser is locked again on resonance so that we have

$$\mathrm{f_{green}} = 2\mathrm{f_{infrared}} + 2\Delta\mathrm{f} + \mathrm{f_{AOM}} = \mathrm{N'} \cdot \mathrm{FSR}.(\mathrm{N} \in \mathbb{Z}) \tag{30}$$

Here, we have $2\Delta f = (\mathrm{N'} - \mathrm{I} - \mathrm{M}) \cdot \mathrm{FSR} = \mathrm{J} \cdot \mathrm{FSR}(\mathrm{J} \in \mathbb{Z})$. So the frequency for main laser, equivalently for squeezing and bright alignment beam, is

$$\mathrm{f}_{infrared} + \Delta\mathrm{f} = \frac{\mathrm{M} + \mathrm{J}}{2} \cdot \mathrm{FSR} \tag{31}$$

Since initially the infrared laser beam is on resonance, we have $\mathrm{M}/2 \in \mathbb{Z}$. Since J can be either even or odd, we need to operate filter cavity when J is even so that $\mathrm{J}/2$ is an integer. Therefore, the infrared beam is still on resonance if there is a laser frequency change of Δf.

However, in the case of a cavity length change $\Delta\mathrm{L}$ after relock, we have FSR change as described of Eq. 6 in the main manuscript. The details of that equation is

$$\begin{aligned} \Delta_{\mathrm{d}}[\mathrm{Hz}] &= (\mathrm{f_{AOM}} \mod \mathrm{FSR'}) \times \mathrm{FSR'}/2 \\ &= \frac{\mathrm{f_{AOM}}}{\mathrm{FSR}}\frac{\Delta\mathrm{L}}{\mathrm{L}}\mathrm{FSR'}/2 \\ &\simeq \frac{\mathrm{f_{AOM}}}{2}\frac{\Delta\mathrm{L}}{\mathrm{L}} \\ &= 1.83 \times 10^5[\mathrm{Hz/m}] \cdot \Delta\mathrm{L}[\mathrm{m}]. \end{aligned} \tag{32}$$

The approximation is made by approximating $\mathrm{FSR'}$ to be FSR.

V. DIFFERENT LENGTH SHIFT SENSED BY GREEN AND INFRARED FROM MIRROR WAVEFRONT ERROR

Here we analyze the filter cavity mirrors wavefront error map by considering green and infrared have different beam sizes. Due to beam size difference, green and infrared sense a different size of mirror. As a result, these different regions can have a slightly different radius of curvature (RoC), averaged mirror height (simply called 'offset' here after), and tilt.

We use FINESSE to estimate how a mirror wavefront deviates from a perfect sphere. FINESSE can center the beam on different mirror positions and extract information about RoC, offset and tilt sensed by these 2 beams. The RoC change influences beam size and the Gouy phase, which directly introduces a phase change of the filter cavity reflected beam. The offset is a differential length change for green and infrared. Finally, a differential tilt between green and infrared introduces differential length change. Since green is always locked on resonance, these differential phase or length changes between green and infrared are infrared detuning changes.

It should be noted that we analyze only wavefront error measured at 633 nm. It was found that multi-layer coating has different phase changes for different wavelengths [7]. Therefore, it is crucial to analyze green with 532 nm map while analyzing infrared with 1064 nm map. The discussion of this section is considered to provide a method with a result not completely accurate.

A. green and infrared differential Gouy phase

We assume the beam position is fixed on one cavity mirror and sense a RoC R_f and scan the position of the beam on the other mirror, which is an array of RoC R. We have g factor

$$\begin{aligned} g_1 &= 1 - L/R_f, \\ g_2 &= 1 - L/R, \end{aligned} \tag{33}$$

where L is the cavity length. The waist size is expressed as

$$\omega_0 = [(\lambda/\pi)^2 \frac{L(R_1 - L)(R_2 - L)(R_1 + R_2 - L)}{(R_1 + R_2 - 2L)^2}]^{\frac{1}{4}} \tag{34}$$

Using g factors, we obtain waist position

$$z_\omega = L \frac{(1 - g_1)g_2}{|g_1 + g_2 - 2g_1 g_2|} \tag{35}$$

In the end, we obtain Gouy phase

$$\phi_g = 2(\arctan \frac{z_\omega}{z_R} + \arctan(\frac{L - z_\omega}{z_R})), \tag{36}$$

where z_R is Rayleigh range $z_R = \pi\omega_0^2/\lambda$. The subtraction of green and infrared Gouy phase array gives the infrared detuning change map as Fig. 6 for end mirror and Fig. 7 for input mirror when green is always kept on resonance.

B. green and infrared differential offset

The offset term of a mirror surface can be considered as a cavity length change. The offset for green and infrared is different when hitting on different positions on the mirror, whose subtraction will cause infrared detuning change as Fig. 8 for end mirror and Fig. 9 for input mirror.

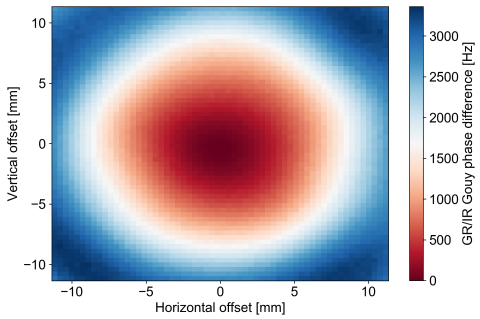

FIG. 6. infrared detuning change caused by green and infrared differential Gouy phase on end mirror.

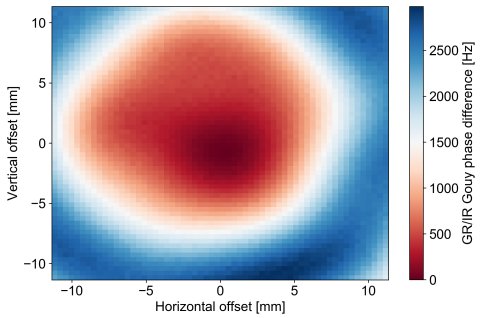

FIG. 7. infrared detuning change caused by green and infrared differential Gouy phase on input mirror.

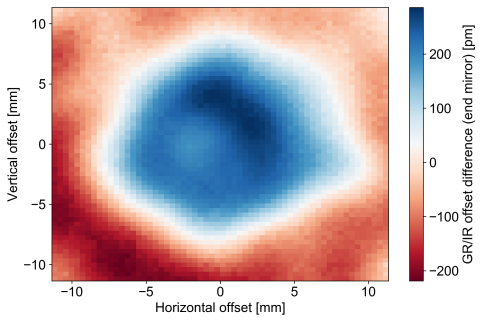

FIG. 8. infrared detuning change caused by green and infrared differential offset on end mirror.

C. green and infrared differential tilt

The differential tilt between green and infrared creates different optical axes for filter cavity. When alignment changes, the differential length will also be introduced. With Eq. 9, we estimated differential green and infrared length change in pitch and yaw direction as Fig. 10 and Fig. 11. From these two figures, if the intra-cavity beam is centered roughly around the mirror center, this effect

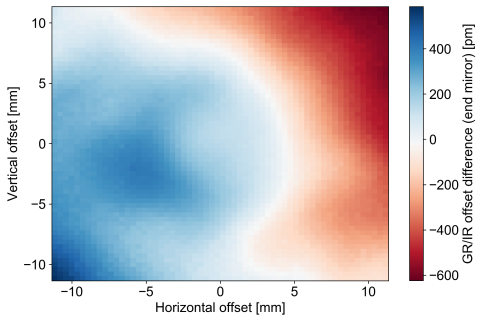

FIG. 9. infrared detuning change caused by green and infrared differential offset on input mirror.

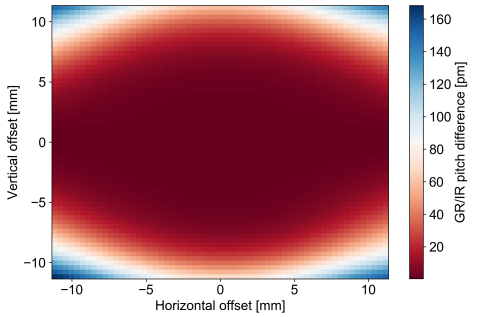

FIG. 10. infrared detuning change caused by green and infrared differential tilt in pitch.

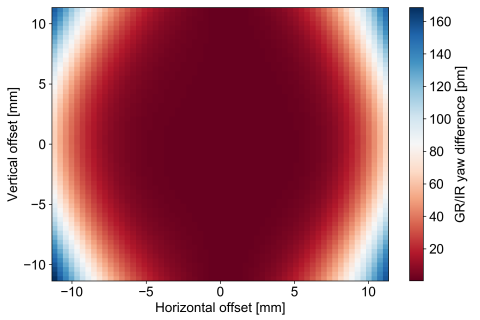

FIG. 11. infrared detuning change caused by green and infrared differential tilt in yaw.

will not introduce considerable detuning change.

VI. FITTING FREQUENCY DEPENDENT SQUEEZING MEASUREMENT FOR FILTER CAVITY DETUNING EXTRACTION

The frequency dependent squeezing gets degradation from classical noise. A model describes such effects is from Ref. [8]. In this model, we consider nine parameters, including generated squeezing level, propagation optical losses, filter cavity optical losses, mode matching between squeezer and filter cavity, mode matching between squeezer and local oscillator, phase noise, filter cavity length locking error, homodyne angle, and filter cavity detuning. Between each measurement, the homodyne angle is changed while other parameters are kept the same. To fit data of frequency dependent squeezing, we used python package 'emcee'[9] by fixing five parameters and setting four parameters to be free in a reasonable range, including generated squeezing level, propagation optical losses, homodyne angle, and filter cavity detuning. The reasonable parameters range is found by fitting data with orthogonal distance regression method. The free parameters are considered to vary because of OPO temperature change, homodyne shot noise level change, homodyne visibility change, filter cavity alignment change and so on. The fixed parameters are either more stable or have negligible influence on the squeezing level.

VII. DETUNING CHANGE AND QUANTUM NOISE REDUCTION

When detectors are operated in broadband resonant sideband extraction mode, the vacuum frequency-dependent rotation imposed by detector can be characterized with just $\Omega_{\rm SQL}$ [8], which implies a matrix

$$\begin{pmatrix} 1 & 0 \\ -(\Omega_{\rm SQL}/\Omega)^2 & 1 \end{pmatrix} \tag{37}$$

to the vacuum fluctuation, where $\Omega_{\rm SQL}$ is the frequency where radiation pressure noise equals to shot noise and Ω is the signal sideband frequency. For example, for KAGRA detector, we have

$$\Omega_{\rm SQL} \simeq \frac{t_{\rm sr}}{1+r_{\rm sr}}\frac{8}{c}\sqrt{\frac{P_{\rm arm}\omega_0}{mT_{\rm arm}}} \tag{38}$$

where $t_{\rm sr}$ and $r_{\rm sr}$ is the signal recycling mirror amplitude transmissivity and reflectivity, c is the speed of light, $\rm P_{arm}$ is the arm cavity circulating power, ω_0 is the frequency of carrier field, m is the mass of test mass mirror, $\rm T_{arm}$ is the input mirror power transmissivity of arm cavity. Taking into account the KAGRA interferometer configuration in Tabel. II, we find $\Omega_{\rm SQL} = 76$ Hz.

To compensate the phase rotation effect as Eq. 37, a losses filter cavity needs to have linewidth $\gamma_{\rm filter\,cavity} = \Omega_{\rm SQL}/\sqrt{2}$ and detuning $\gamma_{\rm filter\,cavity}$. A recent research discussed an optimal filter cavity linewidth and detuning [10]. However, we used our actual filter cavity parameter in this simulation, which is very close to an optimal filter cavity linewidth due to a low level of intra-cavity optical losses. In addition, we found optimal filter cavity detuning in Table. III by manually optimizing binary neutron range.

When filter cavity detuning doesn't match detector optical configuration, we have quantum noise reduction as

TABLE II. Symbols and values for KAGRA interferometer parameters.

Parameter	Symbol	Value
Frequency of the carrier field	ω_0	$2\pi\times$ 282 THz
Arm cavity length	L	3000 m
Arm cavity half-width	$\gamma_{\rm arm}$	$2\pi \times$ 16 Hz
Arm cavity input mirror power transmissivity	$T_{\rm arm}$	0.4 %
Signal recycling mirror power transmissivity	$T_{\rm sr}$	15.36 %
Intra-arm cavity power	$P_{\rm arm}$	400 kW
Mass of each of the test mass mirror	m	22.8 kg

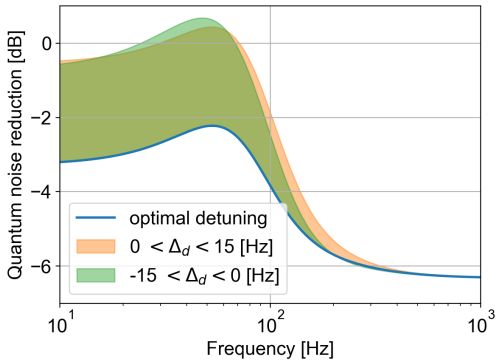

FIG. 12. Quantum noise reduction comparison with filter cavity infrared optimal detuning and detuning change around it by ±15 Hz. Note that the negative value means quantum noise is reduced.

TABLE III. Squeezing degradation parameters

Parameter	Value
Generated squeezing level	9 dB
filter cavity length	300 m
filter cavity intra-cavity optical losses	80 ppm
Squeezing injection optical losses	5 %
Interferometer readout optical losses	5 %
Mode mismatch from squeezer to filter cavity	6 %
Mode mismatch from filter cavity to interferometer	2 %
filter cavity length noise	3 pm
Phase noise	30 mrad
filter cavity detuning	52 Hz

shown in Fig. 12 and Fig. 13. The squeezing degradation parameters are summarized in Table. III. We can see that a detuning change of ±15 Hz can even make quantum noise worse than no-squeezing at some frequencies around tens of Hertz. But when the detuning change is smaller than ±5 Hz, the quantum noise reduction becomes worse by only about 0.5 dB.

[1] Julia Casanueva Diaz. *Control of the gravitational wave interferometric detector Advanced Virgo*. Springer, 2018.

[2] Gerhard Heinzel, Albrecht Rüdiger, Roland Schilling, K Strain, Walter Winkler, J Mizuno, and Karsten Danzmann. Automatic beam alignment in the garching 30-m prototype of a laser-interferometric gravitational wave detector. *Optics communications*, 160(4-6):321–334, 1999.

[3] Andreas Freise and Kenneth Strain. Interferometer techniques for gravitational-wave detection. *Living Reviews in Relativity*, 13(1):1–81, 2010.

[4] Dana Z Anderson. Alignment of resonant optical cavities. *Applied Optics*, 23(17):2944–2949, 1984.

[5] B Canuel, E Genin, M Mantovani, J Marque, P Ruggi, and M Tacca. Sub-nanoradiant beam pointing monitoring and stabilization system for controlling input beam jitter in gravitational wave interferometers. *Applied optics*, 53(13):2906–2916, 2014.

[6] Gerhard Heinzel. TAMA beam centering system. `http://www2.nao.ac.jp/~gw-elog/osl/uploads/2143_20200804154144_galvodocument.pdf`, 1999. [Online; accessed 25-May-2021].

[7] Benoît Sassolas, Marc Bétoule, Nicolas Regnault, Bernard Lagrange, David Hofman, Laurent Balzarini, Laurent Pinard, Danielle Forest, Gianpietro Cagnoli, J-C Cuillandre, et al. High precision metrology for large bandpass filters. In *Advances in Optical and Mechanical Technologies for Telescopes and Instrumentation III*, volume 10706, page 107064E. International Society for Optics and Photonics, 2018.

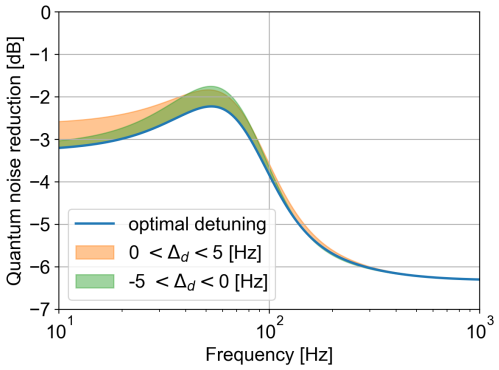

FIG. 13. Quantum noise reduction comparison with filter cavity infrared optimal detuning and detuning change around it by ± 5 Hz.

[8] Patrick Kwee, John Miller, Tomoki Isogai, Lorenzo Barsotti, and Matthew Evans. Decoherence and degradation of squeezed states in quantum filter cavities. *Physical Review D*, 90(6):062006, 2014.

[9] Daniel Foreman-Mackey, David W Hogg, Dustin Lang, and Jonathan Goodman. emcee: the mcmc hammer. *Publications of the Astronomical Society of the Pacific*, 125(925):306, 2013.

[10] Chris Whittle, Kentaro Komori, Dhruva Ganapathy, Lee McCuller, Lisa Barsotti, Nergis Mavalvala, and Matthew Evans. Optimal detuning for quantum filter cavities. *Physical Review D*, 102(10):102002, 2020.